nature portfolio

https://doi.org/10.1038/s41594-021-00626-1

Supplementary information

DNA-loop-extruding SMC complexes can traverse one another in vivo

In the format provided by the authors and unedited

SUPPLEMENTARY INFORMATION

DNA-loop extruding SMC complexes can traverse one another *in vivo*

Hugo B. Brandão[1‡], Zhongqing Ren[2‡], Xheni Karaboja[2], Leonid A. Mirny[1,3*], Xindan Wang[2*]

This PDF file includes:

Supplementary Note 1: Loop Extrusion Simulations
Numpy 1.18.1 was used for most of the calculations below [1].

Lattice set-up: We define the 4033-kb chromosome as a lattice of L = 4040 sites, where each lattice site corresponds to ~1 kb of DNA. The origin of replication is situated at lattice position 0, and the terminus is between lattice positions 1950-2050. Since the genome is circular, the lattice position of monomer 4040 is connected to the first monomer; as such, loop extrusion steps occur with periodic boundary conditions (i.e. a step from lattice site 4040 to 4041 becomes effectively a step from 4040 to 1).

Time steps and rates of extrusion: We use a fixed-time-step Monte Carlo algorithm as in previous work [2]. The 1D extrusion simulations proceed with time-steps equivalent to 1/20th of a second. Loop extruding factors (LEFs) are represented as two motor subunits, which move independently from one another in opposing directions one lattice site at a time [3]. To account for the asymmetric rates of extrusion observed in *B. subtilis* experimentally [4], we introduce direction specific rates: a LEF subunit moving in the *ori*-to-*ter* direction will change lattice sites with a probability 0.05, while in the *ter*-to-*ori* direction it changes with a probability of 0.035 per simulation step. This ensures that in the absence of interactions, the LEFs have an average extrusion rate of ~1 kb/s from *ori* to *ter* and ~0.7 kb/s from *ter* to *ori*. We define the "terminus" at position 2000, which is in the middle of the 1950-2050 region.

***parS*-specific loading rates (i.e. the *parS* loading strength):** We allow LEFs to randomly load at any lattice position. To mimic the effect of biased loading of LEFs at *parS* sites, we make loading at the lattice sites that designated as *parS* sites more probable than non-*parS* sites. For example, to simulate a strain with a *parS* site at the -27˚ position on a chromosome, we designate the lattice site position 3737 (i.e. (360-27)/360*4040 = 3737) to be the *parS* location. We make the relative probability of loading at a *parS* lattice site 4000 times stronger than at non-*parS* sites. Thus, in a simulated strain with one *parS* site, the loading bias at the *parS* site is 4000. Because there are ~4000 non-*parS* sites, ~50% of the LEFs will load at *parS* position; for a strain with two *parS* sites, the total loading bias at *parS* sites is 8000 and 66% of LEFs will bind to *parS* sites; for a strain with three *parS* sites, the total loading bias 12000 and ~75% of LEFs load at *parS*, and so forth.

Spontaneous dissociation rate: This is the basal dissociation rate at which a LEF spontaneously falls off DNA. We fixed the spontaneous dissociation rate at 0.0004 s^{-1}. Details of this choice can be found in "*Finding the optimal model parameters that match experimental data*". For each simulation time step, a random number is drawn between 0 and 1; if the value falls below the basal dissociation probability, then the LEF (i.e. both motor subunits) dissociate from the chromosome and load elsewhere.

Terminus-specific dissociation rate: The lattice sites at the terminus region (i.e. monomers 1950-2050) are given a dissociation rate of 0.0025 s^{-1} (which is roughly ~5-fold of the spontaneous dissociation rate). See "*Finding the optimal model parameters that match experimental data*" below for details.

Facilitated dissociation rate (also called the unloading rate): This is the rate at which a LEF is dissociated from the DNA facilitated by another LEF at the collision. We describe how we determine this rate in "*Finding the optimal model parameters that match experimental data*" below.

Bypassing rate: This is the rate or probability that a LEF bypasses the colliding. We note that there are two LEFs at each collision, and when one LEF bypasses the other, both LEFs will continue extrude DNA. We describe how we found this rate in "*Finding the optimal model parameters that match experimental data*".

Number of LEFs: This is the number of LEFs that are on the chromosome. We systematically varied this number in "*Finding the optimal model parameters that match experimental data*". In our simulations, when a LEF dissociates from the chromosome, it immediately loads back to the chromosome. Therefore, the number of LEFs on the chromosome does not change over time. We note that the loading and dissociation are not uniform along the chromosome. As discussed above, for dissociation there are rates for three different scenarios: spontaneous dissociation, terminus-specific disassociation, and facilitated dissociation; for loading, there is a preference to load at the *parS* site, see "*parS*-specific loading rates", but LEFs may load anywhere on the chromosome.

Rules of LEF interaction (bypassing and unloading): LEFs are deemed to encounter one another when they occupy adjacent lattice sites. We note that each LEF has two subunits that are independently moving on two lattice sites. By default, we do not allow any LEF subunit to take a step onto an occupied site. The only exception is if a LEF "bypasses" another; in this case, LEFs can move to co-occupy the same lattice site. Further steps may proceed unhindered if the adjacent sites are free.

To simulate bypassing and unloading we first define a bypassing probability per simulation time step (i.e. the bypassing rate), *b*, and an unloading probability per simulation time step (i.e. the unloading rate or facilitated dissociation rate), *u ,* where b+u <= 1. Steps are taken following the principles of the Monte Carlo algorithm. At each simulation time step, a random number is drawn between 0 and 1. If the value is above (*b*+*u*), then the subunit location remains unchanged (i.e. no action is taken). If the value is below (*b*+*u*), but above *b,* then the LEF (i.e. both subunits) is marked to unload from the chromosome and re-load at the next time step following the loading rules above. Finally, if the value is below *b*, then the LEF subunit can move forward onto the occupied lattice site. Importantly, we note that at each simulation time step, *all* LEF subunits are updated simultaneously in this way. Moreover, the values *b* and *u*, will be slightly different depending on the direction of movement (i.e. *ori* to *ter,* or *ter* to *ori*, see above).

Loop extrusion equilibration steps: We compute 100,000 initialization steps for the loop extrusion simulations to ensure that the loop statistics have reached a steady-state before creating any contact maps.

Supplementary Note 2: 3D Polymer Simulations

We coupled each of the 1D loop-extrusion simulations to a model of a polymer chain [2] and performed molecular dynamics simulations using Polychrom [5], a Python API that wraps the molecular dynamics simulation software OpenMM [6]. In this coupled model, LEFs act as a bond between the two DNA monomers. These bonds are dynamically updated depending on the position of the LEFs on the lattice. From the polymer simulations, we obtain 3D polymer structures from which we can create contact frequency (Hi-C-like) maps (see below). Polymers are constructed of $L = 4040$ consecutive monomers bonded via the pairwise potential:

$$\mathrm{U}_{\mathrm{bonds}}(r) = \frac{k}{2}(r-b)^2,$$

Where $k = 2k_bT/\delta^2$ is the spring constant (k_b is the Boltzmann constant, T is the temperature, and $\delta = 0.1$ is effectively the bond wiggle distance in monomer units), $r = |r_i - r_j|$ is the spatial

displacement between monomers, and $b = 1$ is the mean distance between monomers in monomer units (typically ~30 nm). Monomers crosslinked by a LEF are held together by the same potential.

To account for excluded volume interactions between monomers, we have a weak polynomial repulsive potential:

$$U_{excl}(r) = \frac{E_{ex}}{E_m}\left(\frac{r}{\sigma}r_m\right)^{12}\left(\left(\frac{r}{\sigma}r_m\right)^{2} - 1\right) + E_{ex}$$

Defined for $r < \sigma = 1.05$, where $r_m = \sqrt{6/7}$, $E_m = 46656/823543$ and $E_{ex} = 1.5k_BT$.

At the start of each simulation, the polymer is initialized as a random walk, with normally distributed velocities such that the total temperature is T. The system thermostat is set with an error tolerance of 0.01. Time steps integration is performed using the "variableLangevin" algorithm, and the collision rate is set to 0.03. Simulations were performed with periodic boundary conditions, where the box size was 27.2 monomer units in each dimension. This box size was set so that the chromosome volume density is 20%, which is within the experimentally expected range (see section below for further details).

Parameterizing the polymer model. We use 1 monomer of 30 nm in diameter, containing 1 kb of DNA locally compacted by supercoiling and other factors. Thus, we have a box dimension of 810 nm by 810 nm by 810 nm. This gives the monomer volume density within the range of ~20%, which has been typical of other simulations in the literature (Le et al, 2013). The volume fraction of DNA within each 30 nm monomer is ~7%. Together this gives 0.07*0.2=0.014 = 1.4% volume fraction of DNA in the system, similar to the volume fraction of about 1% of bacterial DNA in the B. subtilis nucleoid (1.04±0.12 μm in length and 0.82±0.08 μm in diameter). Furthermore, the mean diameter of the otherwise unconfined ring polymer chain of 4000 monomers is 36 monomers which is only slightly bigger than the size of the periodic boundary condition box of 27, so the chain is largely unconfined.

Limitations for the 3D polymer simulations. We note that our polymer simulations allow for chain passing, which mimics the effect of topoisomerases in the cell and also helps to speed up mixing of the chain. This allows us to run shorter simulations and to capture a greater diversity of chromosome conformations. In our simulations, we did not include mechanical feedback between the polymer configurations and LEF dynamics, or model how topological constraints could affect the LEF translocation dynamics. *In vivo*, it is possible that the local polymer configuration (e.g. stretching, looping, or other conformations) has an effect on LEF movement. Since nature or the strength of such constraints *in vivo* is unknown, we did not include them explicitly in our model; however, we note that the effects of chromosome conformation on LEF dynamics (e.g. on the LEF translocation speed) are implicitly included in our model because we used the experimentally determined rate of LEF translocation on the chromosome. Future work may seek to relax these mechanistic assumptions.

Supplementary Note 3: Contact Map Generation from Simulations

Contact maps were obtained from simulations by two different methods: 3D polymer simulations, or a semi-analytical approach [2].

Contact Map Generation from 3D polymer simulations: The contact maps from 3D polymer simulations are displayed in both main text figures and supplemental figures; we used a

distance cutoff radius of 9 monomers (or equivalently ~270 nm) and a minimum of 3,000 chromosome conformations to compute the contact maps. We note that the choice of cutoff radius did not significantly affect the observed contact patterns, but it did change the perceived level of smoothness of the features. After an initial energy minimization and a further 6000 polymer simulation steps, we started recording chromosome conformations. Chromosome conformations were saved every 3000 polymer simulation steps, where each polymer simulation step contained 20 sub-steps of the 1D loop extrusion simulation. For each polymer simulation step, monomers moved by approximately 1 monomer length (i.e. 30 nm).

Contact Map Generation from the semi-analytical approach: In addition to 3D polymer simulations, we generated contact maps semi-analytically [2]. The semi-analytical approach employs a Gaussian approximation to calculate contact probability maps directly from the lattice positions of LEFs. This approach allowed us to swiftly explore a broad range of model parameter values and generate Hi-C-like maps by circumventing the time-intensive 3D polymer simulations. We adapted our approach from a previous study [2] but with an extension to allow for z-loop like structures, which we explain below.

To compute the semi-analytical contact maps, we first create a non-directed graph of connections between monomers. Nodes of the graph represent monomers and edges represent connections between them. The graph contains edges between all nodes with indices (j, j+1); this creates the polymer chain backbone. Since the chromosome is circular, there is also an edge between the first and last node. Additional edges are introduced between all nodes (pairs of monomers) connected by a loop extruding factor. Thus, for a polymer chain of length L monomers with N LEFs, the graph should contain L nodes, and L+N edges. The effective genomic separation between any two monomers (i,j) is obtained by computing the shortest path, *s*, between the monomers; we use Scipy's [7] shortest_path function (SciPy 1.5.0) found in the scipy.sparse.csgraph module to find, *s*. The contact probability between these two points is then evaluated as s^(-3/2).

Contact probability maps were generated from at least 9,480,000 unique pairs of monomers. This represents 3,000 different chromosome conformations (i.e. different conformations of LEFs), and 3160 unique samples from each conformation. For each chromosome conformation, we sampled contact probabilities by drawing a random list of 80 (out of 4040) monomers; we then computed the contact probability (as described above) between all unique monomer pairs (i.e. 80*79/2 = 3160 pairs) and stored this probability into a matrix. By repeating the process for each of the 3,000 chromosome conformations, and averaging the resulting probability matrices, we obtained a population averaged contact probability map.

For exact contact probability calculations, without the shortest path approximation, please see Banigan et al [2]. We note, however, that Banigan et al [2]– while exact – does not account for z-loops (or pseudo-knots formed by LEFs). It is thus not applicable to the simulations with bypassing extrusion. Moreover, while the shortest path approximation could affect the contact probabilities up to a factor of 2^(3/2)≈2.8 (i.e. the effective distance between the furthest points on a loop), it averages to an underestimation of contact frequency by a factor of ~1.5. As such, although we did not use the absolute values of the semi-analytically derived contact probabilities to draw quantitative conclusions about the Hi-C intensities, the semi-analytical maps was used as an exploratory tool to build intuition for the system.

Short-range contacts: To obtain a quantitative match between the contact probability decay curves from simulations and experiments (**Supplementary Figs. 5-7**), we needed to account for the shallow decay of contact probability at short distances (of lengths <60 kb). It was previously

shown in *Caulobacter crescentus* that adding plectonemes of length ~30 kb was sufficient to get a match between polymer simulations and Hi-C data (Le et al, 2013) [17]. As proxy for supercoiling, we added a series of nested loop structures of 45 kb average length to our simulations throughout the genome. They were constructed as follows: First, we generated a sorted list of 90 random integers between 1 and 4040 (corresponding to the lattice site positions). We added edges connecting the first and second, the third and fourth, the fifth and sixth, and so forth. This created a series of loops of average length 45 kb, separated by gaps of length 45 kb. We stored the positions of these additional "bonds" in a list. Then we repeated this process of generating a sorted list of 90 random integers from 1 to 4040 and creating edges. These two lists were appended together. This process produced overlapping loops of length 45 kb, mimicking the effect of supercoils. Finally, we generated new short-range contacts in this way for every 3000 polymer simulation steps, to randomize the short-range contact positions. These imposed contacts did not interfere with the lattice dynamics of the LEFs described above.

Supplementary Note 4: SMC occupancy profiles from simulations

To compute the SMC occupancy profiles from the simulations, we captured at least 3,000 different LEF conformations. The temporal sampling of LEF conformations proceeded identically to the sampling of 3D polymer conformations (see "Contact map generation from simulations" above). To record the LEF occupancies, we created an array of length L=4040 bins (i.e. the same size as the chromosome) and added +1 counts to each bin occupied by each LEF subunit (note that each LEF has two subunits). Thus, if there were 40 LEFs present on the chromosome, then at each sample a total of +80 counts would be added to the array. To directly compare the LEF occupancy profiles to the normalized SMC ChIP-seq experimental data (i.e. ChIP/input), we computed the median ChIP/input value from the SMC ChIP-seq tracks and normalized the LEF occupancy to match the experimental median value. We note that the experimental ChIP-seq plots have peaks which are correlated with highly transcribed genes [4]. These local effects are the center investigation of our previous study and may partially reflect SMC pausing at RNA polymerase [3]. In our simulations, we have not added assumptions for these local effect. Instead, we focus on the overall trend of the SMC enrichment.

Supplementary Note 5: Theory

Relationship between the tilt of Line 1 (or Line 2) and the LEF extrusion speeds between the *parS* sites: In the sections below, we derive the relationship between the bypassing rates, numbers of LEFs and the tilt of Line 1. However, the same procedure can be analogously applied to Line 2 arriving at similar answers.

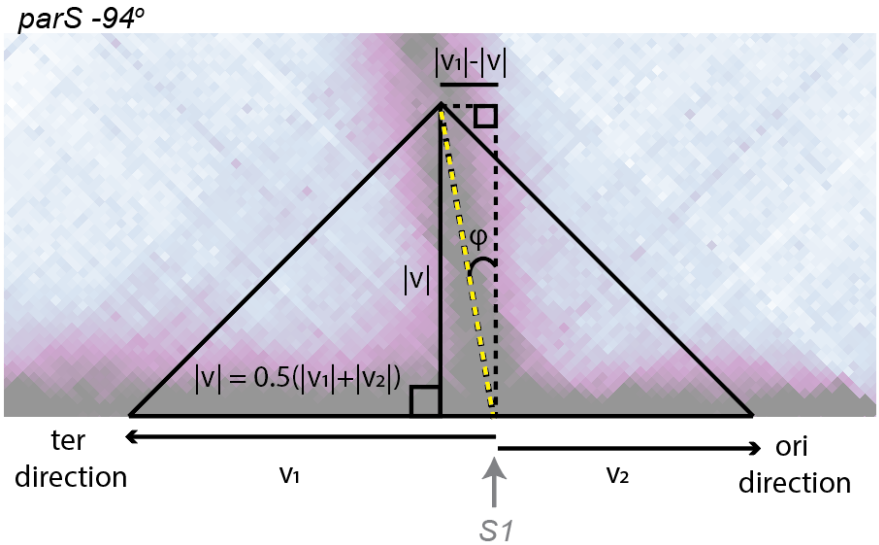

$$\phi = arctan\left(\frac{|v_1| - |v|}{|v|}\right) = arctan\left(\frac{2}{1 + \frac{|v_2|}{|v_1|}} - 1\right)$$

For a strain with a single *parS* site at the *-94°* position (i.e. *S1*), from the diagram and equation above (see also **Extended Data Fig. 2c**), the tilt of Line 1 is related to the relative LEF subunit translocation speeds towards *ori* versus *ter*. By our measurement of $\phi = 9.7^0$, we find that $v_2 \approx 0.707\ v_1$.

For a strain with two *parS* sites at *-94°* and *-59°*, measuring the tilt of Line 1 (see below), we find an angle $\phi = 15.9^0$, or equivalently that $v_3 \approx 0.556\ v_1$.

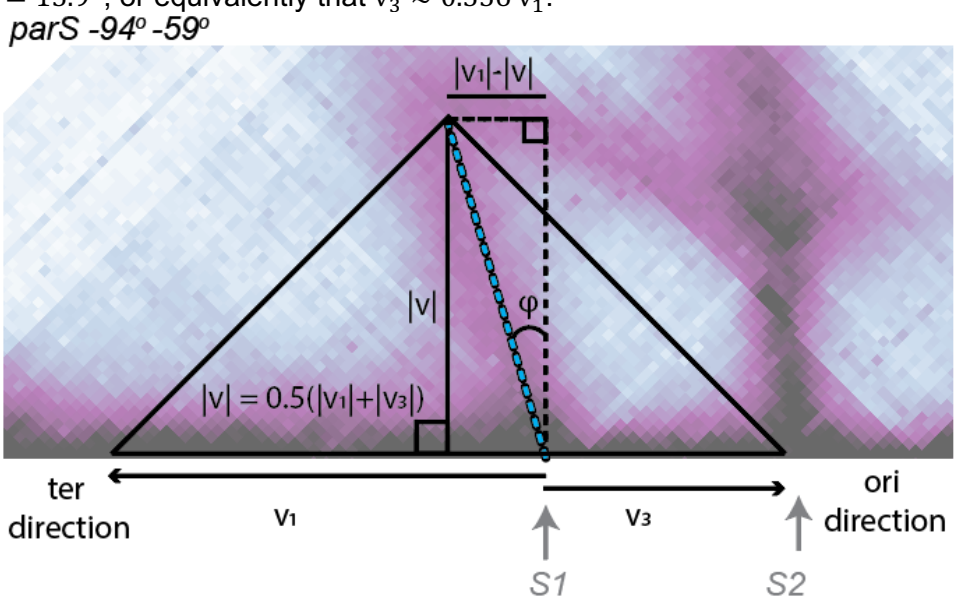

Hence, when there is more than one *parS* site, the average speed of a LEF translocating from *S1* to *S2* decreases by a factor of $v_2/v_3 \approx 1.2$. Moreover, from the reference value $v_1 = 0.83 \pm 0.17$ kb/s from **Extended Data Fig. 2a** and measurements in Wang et al, 2017 [4], we obtain that $v_2 = 0.59 \pm 0.12$ kb/s and $v_3 = 0.46 \pm 0.09$ kb/s.

Relationship between the bypassing rate, number of LEFs and the tilt of Line 1: We can use the measured speeds v_2 and v_3 to estimate the average bypassing rate with a simple model: Consider a LEF subunit translocating a distance *d* from the *parS* site *S1* towards *S2*. We can define the time, τ, as the time it takes to move one lattice site of length $l_0 = 1$ kb, if the adjacent lattice site is unoccupied. We define τ_b as the time to bypass a lattice site occupied by another LEF. If, on average, the LEF subunit travelling from *S1* to *S2* encounters n other LEF subunits, then the total time, T_3 to cross the distance *d* is:

$$T_3 = \left(\frac{d}{l_0} - \mathrm{n}\right)\tau + n \cdot \tau_b$$

We can re-arrange the equation to obtain:

$$\tau_b = \frac{T_3}{n} - \frac{\tau}{n}\left(\frac{d}{l_0} - \mathrm{n}\right).$$

Noting that since $T_3 = d/v_3$ and $\tau = l_0/v_2$, then:

$$\tau_b = \frac{d}{n \cdot v_3} - \frac{d}{n \cdot v_2}\left(1 - \mathrm{n} \cdot \frac{\mathrm{l}_0}{\mathrm{d}}\right).$$

This helps constrain the parameter space for the search of best-fit parameters since the number of LEFs and the bypassing rate are linearly dependent on one another.

Moreover, we see that the ratio of the bypassing rate to the number of LEFs per chromosome is approximately constant. For $\frac{\mathrm{l}_0}{\mathrm{d}} n \ll 1$, as reasonably expected for $n < 100$ (i.e. less than 200 LEFs/chromosome), then:

$$\tau_b \mathrm{n} \approx d\left(\frac{1}{v_3} - \frac{1}{v_2}\right) \approx (188 \pm 53) \text{ LEF seconds,}$$

where we used known values: $d = 392$ kb for the distance between the two *parS* sites (in the -94° -59° strain) and the speeds $\mathrm{v}_2 = 0.59 \pm 0.12$ kb/s and $v_3 = 0.46 \pm 0.09$ kb/s.

Estimating the bypassing rate from the number of SMC complexes: We can calculate the bypassing rate, τ_b, if we can estimate the number of LEFs, n, that a LEF is expected to encounter on its transit from *S1* to *S2* using the relation $\tau_b \approx 188/\mathrm{n}$ seconds derived above.

For this calculation, we will need to know the number of LEFs moving from S2 to S1 when extrusion from *S1* begins; additionally, we will need to know the number of LEFs that bind to S2 after extrusion from *S1* has begun. Thus,

$$n \approx n_{\text{that will bind}} + n_{\text{already present}}.$$

To calculate $n_{\text{that will bind}}$, we will need to know the average time, T_3, that it takes a LEF to cross the distance d (from *S1* to *S2*) and the loading rate, k_{load}, at the *S2 parS* site. It follows that:

$$n_{\text{that will bind}} \approx T_3 k_{load}.$$

The value $\mathrm{T}_3 = d/v_3 \approx 180 \pm 35\ s$, where *d* is the distance between the two *parS* sites (i.e. 392 kb) and v_3 is the average extrusion speed from *S1* to *S2* calculated above. We can calculate k_{load} from the total number of LEFs per chromosome, *N*, and the dissociation rate, k_d, of LEFs using the relation:

$$k_{load} = 0.5 \cdot N \cdot k_d$$

The number of LEFs, *N*, is estimated to be $N = (70 \pm 38)/q$ LEFs/chromosome where *q*=1 if LEFs are monomers of SMC complexes, or *q*=2 if dimers (see **Extended Data Fig. 8b**). The factor of 0.5 in k_{load} arises if we assume that *S1* and *S2* have equal likelihood of loading the LEF.

The dissociation rate, k_d, can be estimated from the average time it takes a LEF subunit to reach the terminus. As a first approximation, we can assume that a LEF immediately dissociates from the chromosome if any subunit reaches the terminus at genome position ~2000 kb; this is an acceptable assumption since experimentally SMCs do not accumulate at *ter* [4]. After dissociating from *ter*, the LEF may re-load at either *S1* or *S2* or elsewhere according to *parS*-specific loading rate. LEFs loaded at *S1* travel a distance of ~980 kb to reach *ter* and take approximately $(1180 \pm 241)\ s$. LEFs loaded at *S2* travel a total distance of ~1372 kb to reach the terminus and take approximately $(1845 \pm 532)\ s$. Thus, the average dissociation rate (per LEF), is then:

$$k_d \approx 0.5 \cdot (1845 + 1180)^{-1} s^{-1} = (0.023 \pm 0.014) s^{-1}$$

and

$$n_{\text{that will bind}} \approx 0.5 \cdot T_3 \cdot N \cdot k_d$$

Combining all the above values and propagating the uncertainties, we obtain the estimate for the number of LEFs encountered as:

$$n_{\text{that will bind}} \approx (4 \pm 3)/q \ \ LEFs.$$

Next, we compute the number of LEFs moving from *S2* to *S1* that were already present in the segment between the *parS* sites at the time the extrusion from *S1* began. We use the distance-weighted average:

$$n_{\text{already present}} \approx 0.5 \cdot N \cdot (392\text{kb}/1372\text{kb})/\text{q} \approx (10 \pm 5)/q\ LEFs$$

Finally, we obtain:

$$n \approx (14 \pm 6)/q \ \ LEFs.$$

$$\tau_b \approx (188 \pm 53)/(14 \pm 6)\text{q}^{-1}\text{seconds}$$

Thus, if a LEF is made of a dimer of SMC complexes, $\tau_b = \ 26\ \pm 19\ s$; if a LEF is made of a monomer of SMC complexes, $\tau_b = \ 13\ \pm 9\ s$. These values are in good agreement with the average bypassing time obtained by 3D polymer simulations of $\tau_b = (20 \pm 10)$ s, and measurements of the bypassing time obtained *in vitro* of ~8 seconds [8].

The frequency of nested doublet interactions is controlled by the ratio of bypassing rates to unloading rates: Nested doublet configurations (**Fig. 2a**) occur when a LEF from one *parS* site (e.g. *S1*) extrudes past the other site (e.g. *S2*) followed by a LEF loading event (i.e. at *S2*). The frequency at which LEFs will enter into this configuration will depend on the bypassing and unloading rates as LEFs encounter one another. If the bypassing rate is $k_b = \tau_b^{-1}$ and the unloading rate is $k_u = \tau_u^{-1}$ (i.e. due to collisions), then the probability that a LEF translocating from the *S1* site manages to reach the *S2* site (neglecting the spontaneous dissociation rate) is given by:

$$P = \left(\frac{k_b}{k_b + k_u}\right)^n \approx e^{-\frac{k_u}{k_b}n} \ = \ e^{-\frac{\tau_b}{\tau_u}n}.$$

Where n is the expected number of encounters that a LEF translocating from *S1* will have with other LEFs on its way to *S2* (see calculation above).

From the relative intensity of Line 3 and Line 4 (from Hi-C data), we estimate that $P \approx 0.5$. Using the values obtained above for n, it follows that $\tau_u \approx 20\tau_b$, meaning that the bypassing rate is 20-fold higher than the unloading rate.

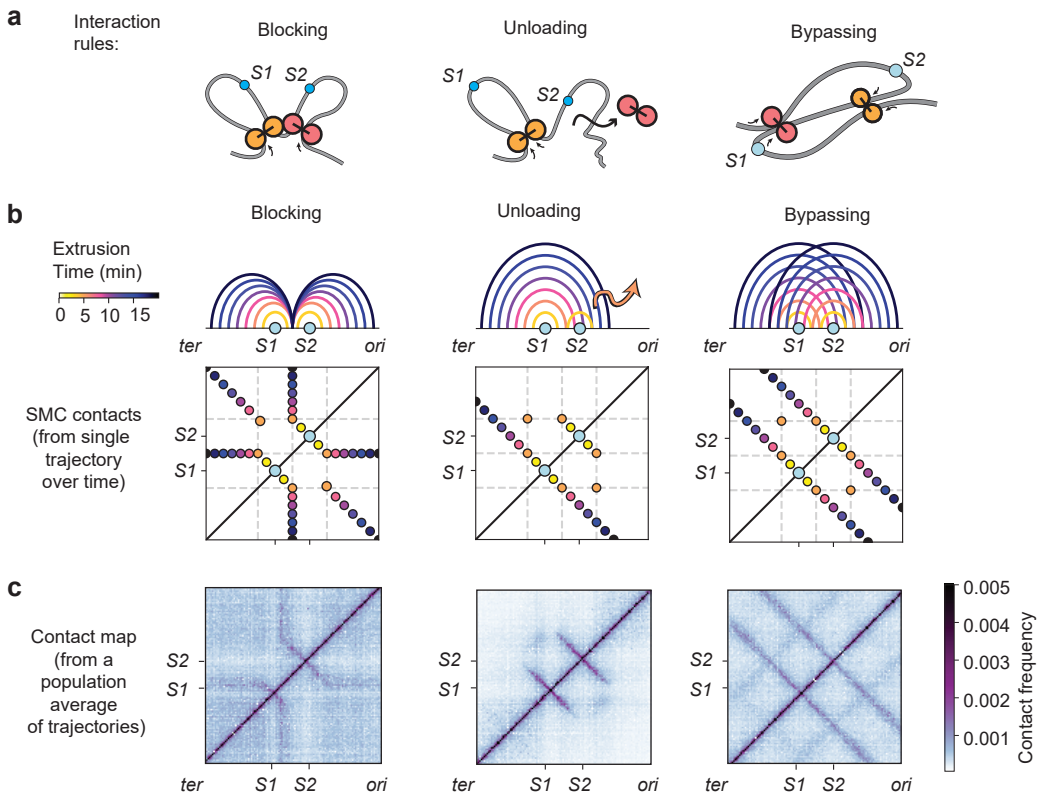

Supplementary Figure 1: Intuition building for interaction rules (case of equal rates). **(a)** Example of how collision doublet conformations form Line 3. *Top row*: arch diagrams showing the time-course of SMC complexes extruding DNA from their *parS* sites (S1 and S2) up to the point of collision. *Middle row*: 2D traces of the extrusion trajectories; each dot shows the genomic coordinates bridged by a loop extruder at various where the time is indicated the color. The colors depict a time-axis, and for any given point in time, in each cell, the SMC complex creates a single point-like interaction along Lines 1 or Line 2; if SMCs collide, they further create a third point-like interaction. The combination of point-like interactions from many cells gives rise to the observed Line 3. Other lines are explained similarly. *Bottom row*: schematic showing the loops formed at the point of collision. **(b)** Schematic of the interaction rules for the case where loop extruding factors extrude with equal rates away from their loading sites. **(c)** Arch diagrams corresponding to the genomic positions bridged by single loop extruders over time; *top row*: colours of each arch correspond to a specific time after loading of the extruder on the genome; *bottom row*: 2D representation of the trajectories. **(d)** Hi-C like contact map resulting from a population average over many extruder trajectories; this illustrative map was generated from a loop extrusion simulation coupled to the semi-analytical approach[11] to generating contacts (see **Supplementary Note 3**), with N=20 loop extruders on the genome.

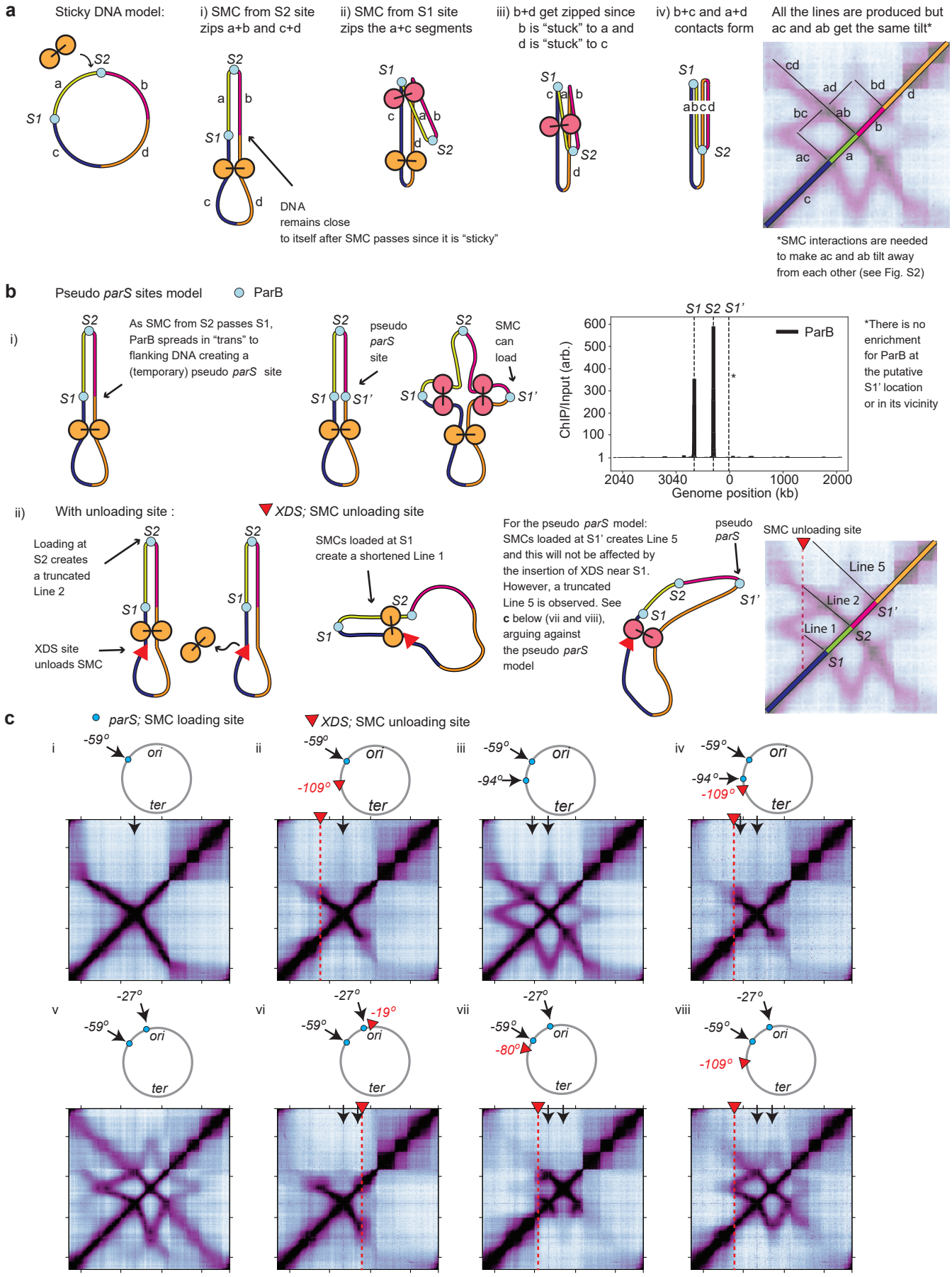

Supplementary Figure 2: (legend on the following page)

Supplementary Figure 2: Alternative models ruled out – part 1. (a) Sticky DNA model. DNA segments (a and b; c and d) stay together after SMC complexes loaded at *S2* pass by. Then when a new SMC complex loads at *S1*, as it generates interactions between segments a and c, it also generates interactions between a and d, b and c because ab and cd are stuck together. Although this could fold the chromosome into a star-shaped pattern and can generate all the lines observed in the Hi-C map, this model does not produce the necessary and observed "tilting" of the lines (e.g. ac and ab) away from each other. The tilting of Hi-C traces in strains with multiple *parS* sites relative to strains with single *parS* sites indicate non-trivial interactions between SMC complexes (leading to slowing down of SMC translocation). **(b)** Pseudo-*parS* sites model. When SMC complexes loaded from *S2* pass *S1*, ParB at *S1* spreads onto the mirror chromosome arm at *S1*' creating a temporary/pseudo loading site for SMC complexes. This model would predict some accumulation of ParB at the pseudo-*parS* (S1') site. However, **(i)** in ChIP-seq experiments, ParB accumulation at the *S1*' site is not visible for a strain with *parS* at -27° and -59° and, **(ii)** this model would predict that the creation of Line 5 would be largely unperturbed in the presence of an SMC unloading site placed between *ter* and the *parS* site at *S1*. However, we see that, **(c)** the placement of an SMC complex unloading site disrupts the star-shaped chromosome interactions both near the unloading site and very far from the site (i.e. both the bottom and the top of the star-shape become clipped). These experiments provide strong support to the idea that Lines 4 and 5 require interactions between SMC complexes that are formed by SMCs loaded at one *parS* site travelling all the way to the adjacent *parS* site and forming nested configurations (e.g. main text **Fig. 2a**).

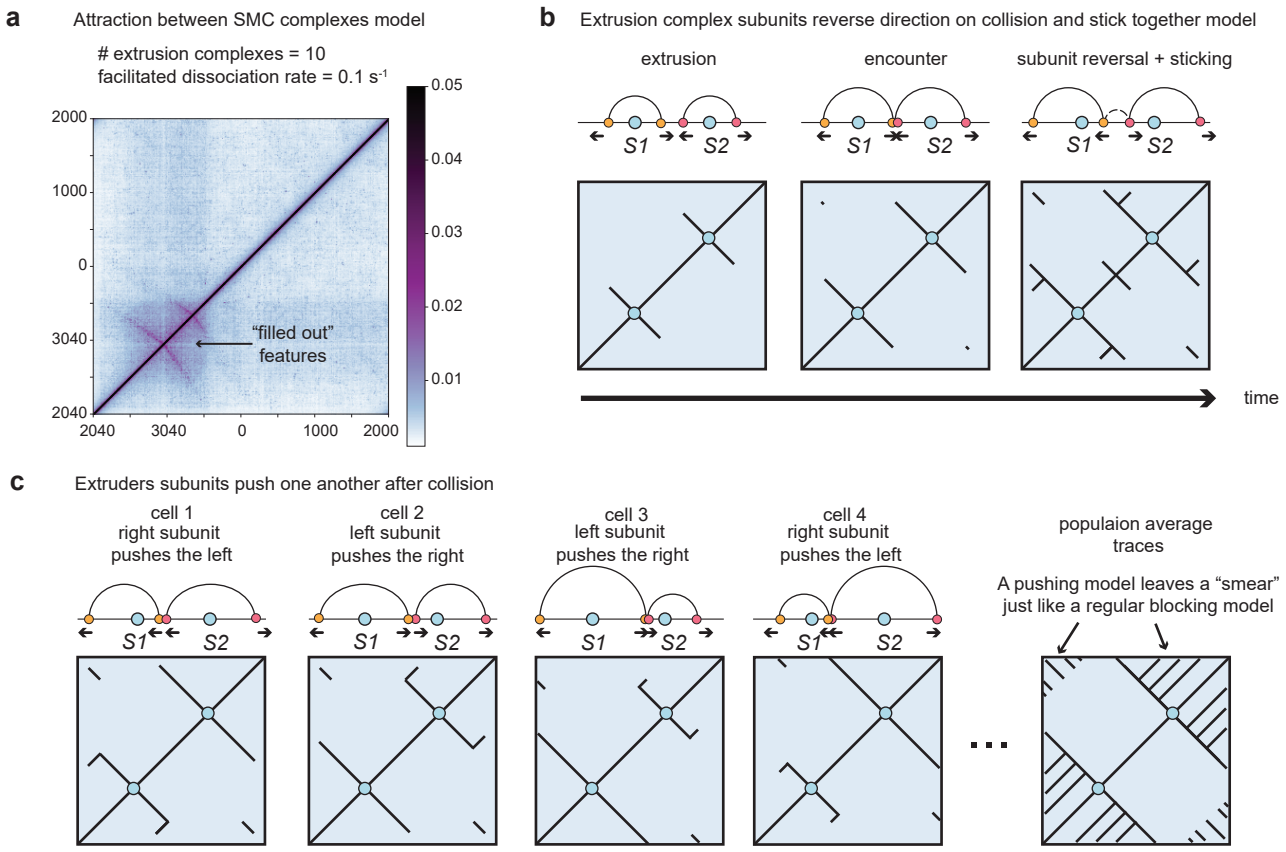

Supplementary Figure 3: Alternative models ruled out – part 2. (a) 3-D attraction between SMC complexes. If SMC complexes translocate on different DNA segments are randomly attracted by 3D attractions to each other, the emergent patterns do not resemble a complete star-shape (e.g. **Extended Data Fig. 3**), and features emerge as smears as opposed to lines "hollow". The shown map corresponds to N=10 extruders and k_u=0.1 s^{-1} and was computed with the semi-analytical model[11]; the strong attraction was created by adding extra random harmonic bonds between half of the extruders. **(b)** Reversal and sticking upon collision. When two DNA extruders meet, they stick to each other and both the inner subunits of the extrusion complex reverse direction. The sticking interaction generates new interactions depicted as a "dashed" line between the orange and magenta subunits in the top, rightmost panel. Bottom panels depict the time-averaged 2D representation of the trajectories. This model produces lines on the interaction maps that are not seen experimentally. **(c)** Subunit pushing upon collision. When two DNA extruders meet, one subunit dominates the other and pushes the other back. This model produces lines on the interaction maps that are not seen experimentally.

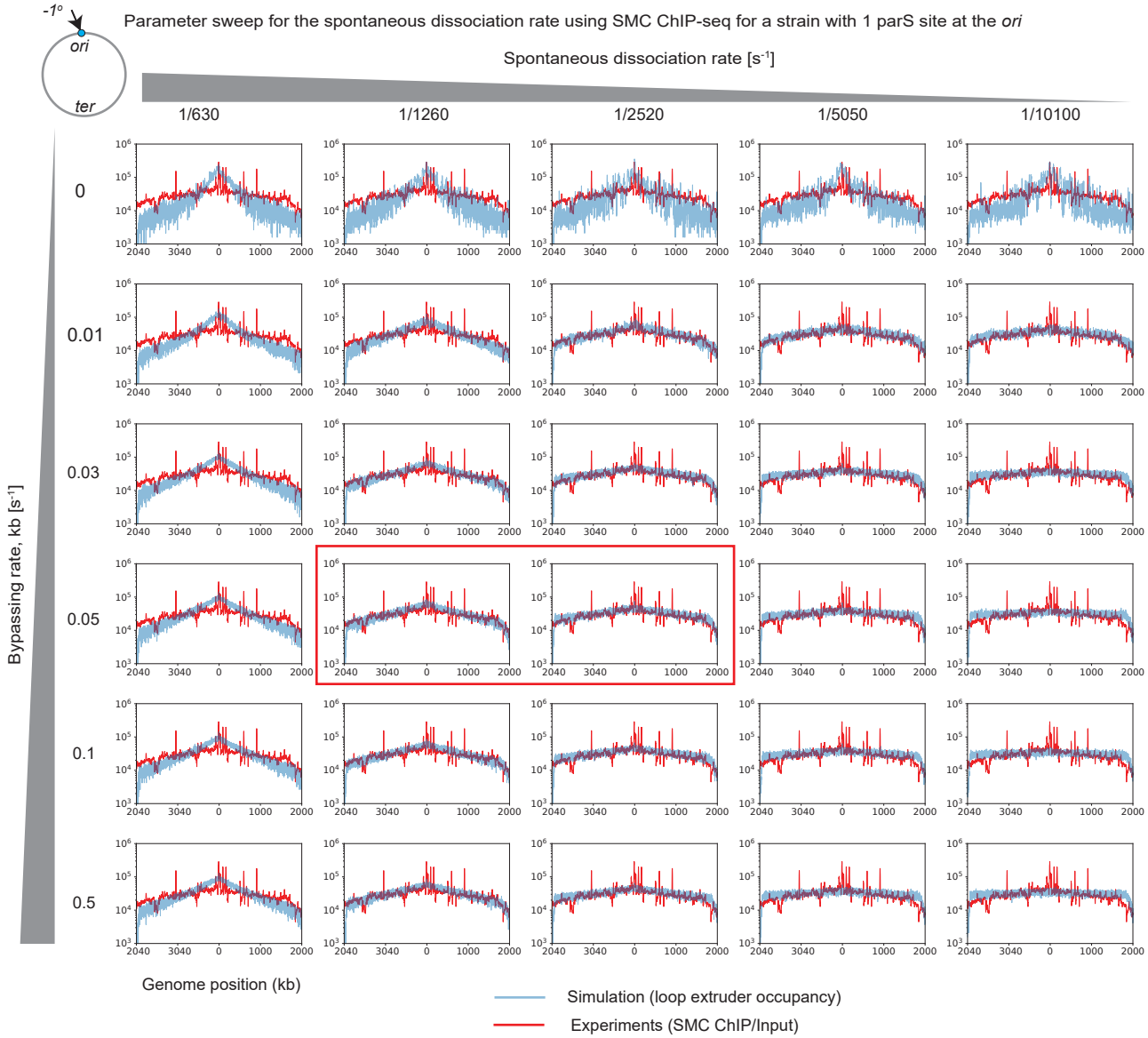

Supplementary Figure 4: The spontaneous dissociation rate controls SMC complex abundance as a function of distance from the *parS* site. To obtain an estimate of the spontaneous dissociation rate, we compared the input-normalized experimental SMC ChIP-seq profile to the occupancy profile of loop extruders from simulation. We used a model where extrusion complexes can bypass one another and dissociate spontaneously, and where the facilitated unloading rate (from SMC complex encounters was set to zero). The experimental data was obtained from a strain with a single *parS* site near the origin (Wang et al, 2017), and was compared to a model with a *parS* site also at the -1° position. Notably, when the bypassing rate was 0 s^{-1}, loop extruders accumulate strongly near the loading site for all values of the dissociation rate (i.e. top row). Additionally, if the dissociation rate was too high ($\gtrsim$ 1/630 s^{-1}) or too low ($\lesssim$ 1/5050 s^{-1}), then the occupancy profile was too steep or too shallow, respectively. The optimal profiles (shown in the black box) were obtained for the bypassing rate near 0.05 s^{-1} and dissociation rates 1/1260 s^{-1} and 1/2560 s^{-1}. We chose 1/2560 s^{-1} to be the default for all simulations thereafter as it also gave a better agreement with the Hi-C contact maps.

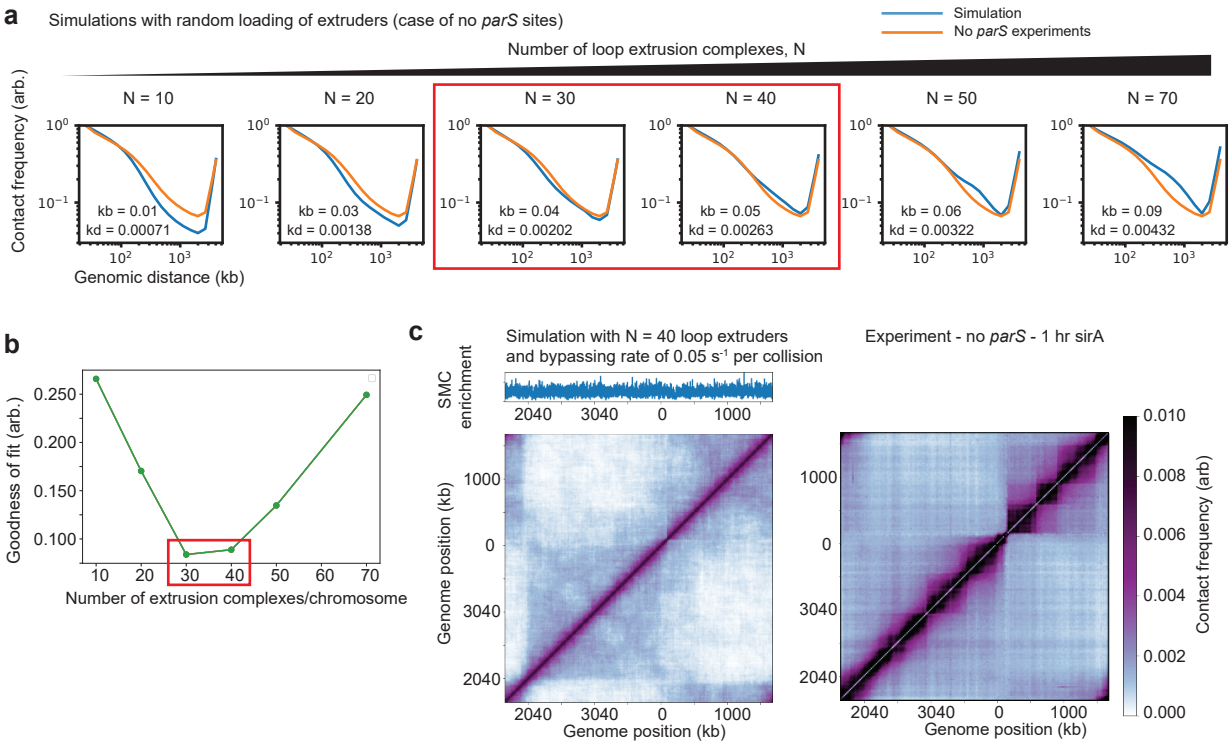

Supplementary Figure 5: Determining the number of loop extruders per chromosome by matching contact probability decay curves. (a) Comparison of the contact probability decay curve of 3D polymer simulations with bypassing rates and varying numbers of extruders (as specified). The bypassing rate was constrained theoretically in relation to N, plectonemes were created with an average length of 45 kb and contacts were computed using a 9 monomer cutoff radius (i.e. ~ 9 kb) (see **Supplemental Note** sections on *3D Polymer simulations* and also *Contact Map Generation from Simulations*). **(b)** Goodness of fit of the simulated contact probability decay curves (from **(a)**) as compared to the experimental curve. The best fit (minimum of the goodness of fit) occurs for ~30-40 extruders per chromosome as denoted by the red box. **(c)** Contact map and SMC enrichment profile for the simulation with N = 40 extrusion complexes (left) and experimental contact map (right).

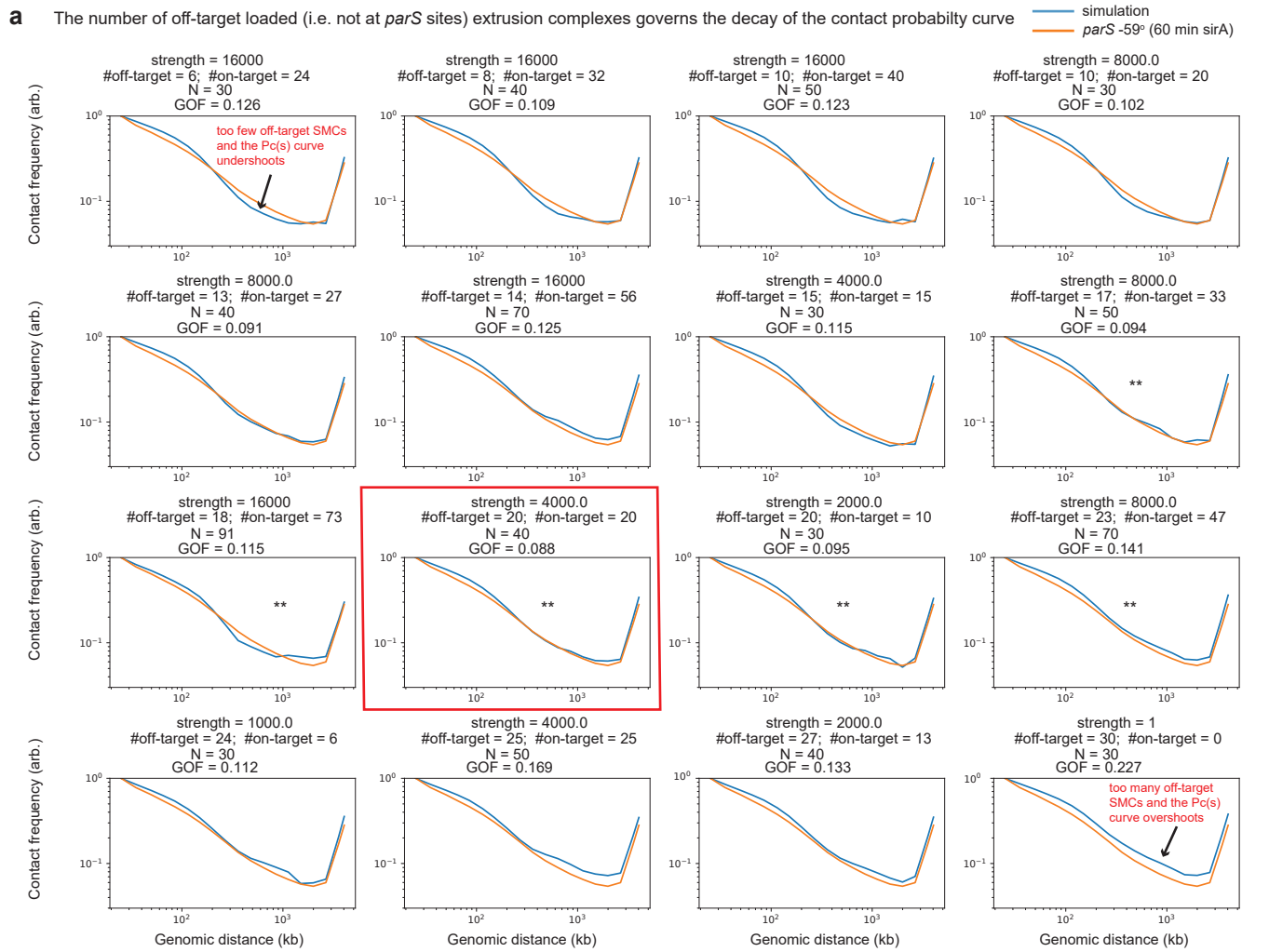

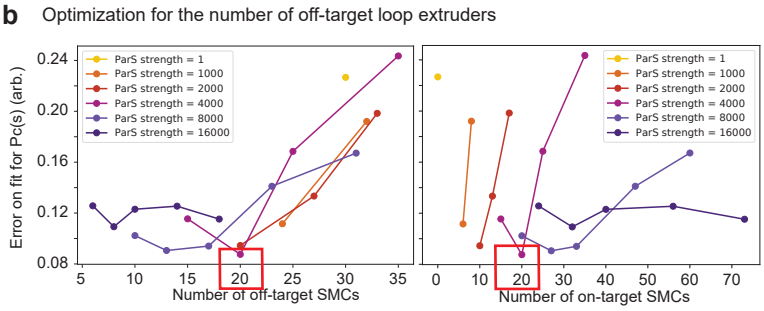

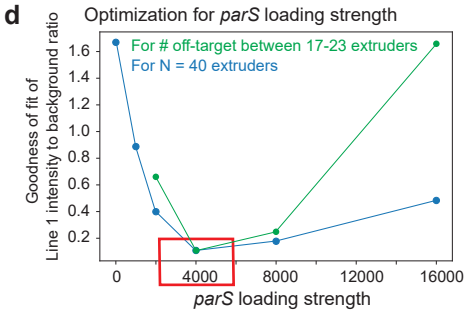

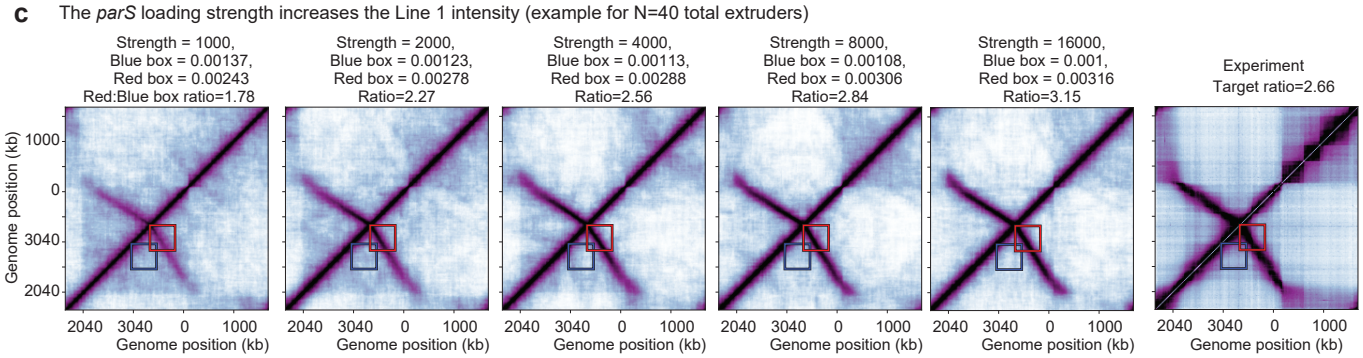

Supplementary Figure 6: (legend on the following page)

Supplementary Figure 6: Determining the basal (non *parS* site to *parS* site) loading rate of SMCs using Hi-C from strains with a single *parS* site. Contact probability decay curves are shown for a parameter sweep of simulations where the rate of loading between *parS* and non-*parS* sites was varied. 3D polymer simulations were performed for a single *parS* site at the -59º position. Plectonemes of length 45 kb were included in these simulations to reproduce the experimental short-range contact probability. The bypassing rate was constrained theoretically in relation to N (see **Supplementary Note 5**). The strength of the *parS* site is shown above each graph denoted "strength", indicating the relative likelihood that an SMC will load at the *parS* site monomer versus any other of the 4040 simulation monomers. The average number of extruders loaded at *parS* site versus off *parS* sites is indicated by "on target" and "off target", respectively. The total number of extruders present in a simulation is indicated by the value N = "#on-target" + "#off-target". The red box highlights the best matching curve for the simulations as determined by the goodness of fit metric (GOF) described in the **Methods**. Notably, we found that the number of off-target extruders were the biggest determinant for the shape of the Pc(s) curves. **(b)** The goodness of fit curves for the Pc(s) curves, displayed as a function of the number of off-target or on-target extruders. The most optimal simulation parameters are shown boxed in red. **(c)** Example simulated Hi-C maps showing that the *parS* strength increases the intensity of Line 1. The red and blue boxes are used to compute the relative intensity of Line 1 to the background contact probability values. The target ratio of the Red:Blue box intensities is 2.66 as measured on the experimental Hi-C map. **(d)** The *parS* strength was optimized by comparing the Line 1 intensity (as measured by the Red:Blue box ratio) of simulations to experiments. We show that the most optimal *parS* strength was found to be 4000, irrespective of whether the number of extruders was fixed (e.g. at N=40), or the number of off-target extruders was kept in the range of 17-24. Thus, the best matched *parS* site monomer strength has a value of 4000-fold more than non-*parS* sites indicating that with one *parS* site present on the genome, the SMC complexes loaded ~50% at the *parS* site and 50% elsewhere.

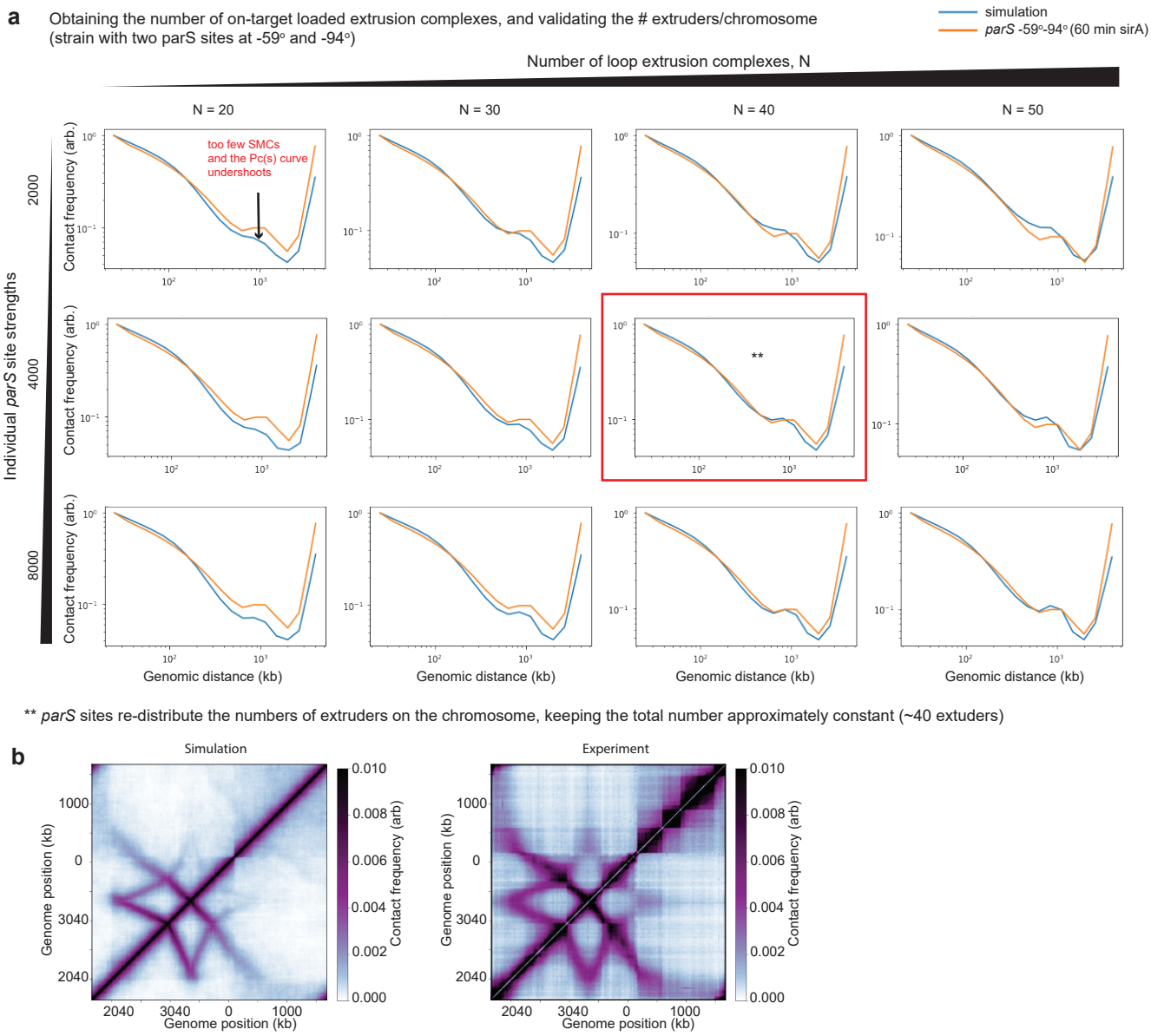

Supplementary Figure 7: Verification and validation of the numbers of extruders present per chromosome and the *parS* loading rate. (a) Using the values identified for N in **Supplementary Figs. 5, 6** and *parS* strength in **Supplementary Fig. 6**, we obtain an excellent match to the contact probability decay curve for the strain harbouring two *parS* sites at -59° and -94°. We see that with two parS sites present on the genome, the SMC complexes load preferentially 66% at the *parS* sites and 33% elsewhere. **(b)** Comparison of the simulated and experimental Hi-C maps corresponding for the conditions and parameters shown in the red box in **a**.

Supplementary Table 1. Next-Generation Sequencing samples used in this study

figure	sample	data type	GEO accession number
Figure 1c (left)	301_Wang_HiC_BWX4476_1mM_060m	Hi-C	GSM4698368
Figure 1c (center)	302_Wang_HiC_BWX4475_1mM_060m	Hi-C	GSM4698369
Figure 1c (right)	303_Wang_HiC_BWX4463_1mM_060m	Hi-C	GSM4698370
Figure 1d (top, 0 min)	304_Wang_HiC_BWX4493_xyl30m_1mM_00m	Hi-C	GSM4698371
Figure 1d (top, 10 min)	305_Wang_HiC_BWX4493_xyl30m_1mM_10m	Hi-C	GSM4698372
Figure 1d (top, 15 min)	306_Wang_HiC_BWX4493_xyl30m_1mM_15m	Hi-C	GSM4698373
Figure 1d (top, 20 min)	307_Wang_HiC_BWX4493_xyl30m_1mM_20m	Hi-C	GSM4698374
Figure 1d (top, 25 min)	308_Wang_HiC_BWX4493_xyl30m_1mM_25m	Hi-C	GSM4698375
Figure 1d (top, 30 min)	309_Wang_HiC_BWX4493_xyl30m_1mM_30m	Hi-C	GSM4698376
Figure 1d (middle, 0 min)	310_Wang_HiC_BWX4491_xyl30m_1mM_00m	Hi-C	GSM4698377
Figure 1d (middle, 10 min)	311_Wang_HiC_BWX4491_xyl30m_1mM_10m	Hi-C	GSM4698378
Figure 1d (middle, 15 min)	312_Wang_HiC_BWX4491_xyl30m_1mM_15m	Hi-C	GSM4698379
Figure 1d (middle, 20 min)	313_Wang_HiC_BWX4491_xyl30m_1mM_20m	Hi-C	GSM4698380
Figure 1d (middle, 25 min)	314_Wang_HiC_BWX4491_xyl30m_1mM_25m	Hi-C	GSM4698381
Figure 1d (middle, 30 min)	315_Wang_HiC_BWX4491_xyl30m_1mM_30m	Hi-C	GSM4698382
Figure 1d (bottom, 0 min)	316_Wang_HiC_BWX4492_xyl30m_1mM_00m	Hi-C	GSM4698383
Figure 1d (bottom, 10 min)	317_Wang_HiC_BWX4492_xyl30m_1mM_10m	Hi-C	GSM4698384
Figure 1d (bottom, 15 min)	318_Wang_HiC_BWX4492_xyl30m_1mM_15m	Hi-C	GSM4698385
Figure 1d (bottom, 20 min)	319_Wang_HiC_BWX4492_xyl30m_1mM_20m	Hi-C	GSM4698386
Figure 1d (bottom, 25 min)	320_Wang_HiC_BWX4492_xyl30m_1mM_25m	Hi-C	GSM4698387
Figure 1d (bottom, 30 min)	321_Wang_HiC_BWX4492_xyl30m_1mM_30m	Hi-C	GSM4698388
Figure 2a, c	303_Wang_HiC_BWX4463_1mM_060m	Hi-C	GSM4698370
Figure 3a (column 1)	322_Wang_HiC_BWX4462_1mM_060m	Hi-C	GSM4698389
Figure 3a (column 2)	323_Wang_HiC_BWX4479_1mM_060m	Hi-C	GSM4698390
Figure 3a (column 3)	324_Wang_HiC_BWX4480_1mM_060m	Hi-C	GSM4698391
Figure 3a (column 4)	325_Wang_HiC_BWX4481_1mM_060m	Hi-C	GSM4698392
Figure 3a (column 5)	326_Wang_HiC_BWX4883_1mM_060m	Hi-C	GSM4698393
Figure 3a (column 6)	327_Wang_HiC_BWX4482_1mM_060m	Hi-C	GSM4698394
Figure 3a (column 7)	328_Wang_HiC_BWX4892_1mM_060m	Hi-C	GSM4698395
Figure 3b (row 1)	329_Wang_HiC_BWX4927_1mM_060m	Hi-C	GSM4698396
Figure 3b (row 2)	330_Wang_HiC_BWX5066_1mM_060m	Hi-C	GSM4698397
Figure 3c	333_Wang_ChIPSMC_BWX4462_1mM_060m	ChIP-seq	GSM4698400
Figure 3c	336_Wang_input_BWX4462_1mM_060m	WGS	GSM4698403
Figure 4a (column 1)	322_Wang_HiC_BWX4462_1mM_060m	Hi-C	GSM4698389
Figure 4a (column 2)	331_Wang_HiC_BWX4462_1mM_090m	Hi-C	GSM4698398
Figure 4a (column 3)	332_Wang_HiC_BWX4462_1mM_120m	Hi-C	GSM4698399
Figure 4b (row 1)	333_Wang_ChIPSMC_BWX4462_1mM_060m	ChIP-seq	GSM4698400
Figure 4b (row 2)	334_Wang_ChIPSMC_BWX4462_1mM_090m	ChIP-seq	GSM4698401
Figure 4b (row 3)	335_Wang_ChIPSMC_BWX4462_1mM_120m	ChIP-seq	GSM4698402
Figure 4b (row 1)	336_Wang_input_BWX4462_1mM_060m	WGS	GSM4698403
Figure 4b (row 2)	337_Wang_input_BWX4462_1mM_090m	WGS	GSM4698404
Figure 4b (row 3)	338_Wang_input_BWX4462_1mM_120m	WGS	GSM4698405
Figure 5a (left)	330_Wang_HiC_BWX5066_1mM_060m	Hi-C	GSM4698397
Figure 5a (middle)	361_Wang_HiC_BWX5066_1mM_090m	Hi-C	GSM4698428
Figure 5a (right)	362_Wang_HiC_BWX5066_1mM_120m	Hi-C	GSM4698429
Figure 5B (left)	367_Wang_ChIPSMC_BWX5066rep2_1mM_060m	ChIP-seq	GSM4698434
Figure 5b (middle)	368_Wang_ChIPSMC_BWX5066rep2_1mM_090m	ChIP-seq	GSM4698435
Figure 5b (right)	369_Wang_ChIPSMC_BWX5066rep2_1mM_120m	ChIP-seq	GSM4698436
Figure 5b (left)	370_Wang_input_BWX5066rep2_1mM_060m	WGS	GSM4698437
Figure 5b (middle)	371_Wang_input_BWX5066rep2_1mM_090m	WGS	GSM4698438
Figure 5b (right)	372_Wang_input_BWX5066rep2_1mM_120m	WGS	GSM4698439

figure	sample	data type	GEO accession number
Figure 6a (left)	363_Wang_HiC_BWX4359_1mM_060m	Hi-C	GSM4698430
Figure 6a (middle)	364_Wang_HiC_BWX4359_1mM_090m	Hi-C	GSM4698431
Figure 6a (right)	365_Wang_HiC_BWX4359_1mM_120m	Hi-C	GSM4698432
Extended Data Figure 1b (left)	29_Rudnerlab_HindIII_HiC_BWX3221 (GSE68418) [9]	Hi-C	GSM1671427
Extended Data Figure 1b (middle)	08_Wang_HiC_BWX3377 (GSE85612) [4]	Hi-C	GSM2279747
Extended Data Figure 1b (right)	339_Wang_HiC_BWX4428	Hi-C	GSM4698406
Extended Data Figure 2a (row 1, column 1)	310_Wang_HiC_BWX4491_xyl30m_1mM_00m	Hi-C	GSM4698377
Extended Data Figure 2a (row 1, column 2)	311_Wang_HiC_BWX4491_xyl30m_1mM_10m	Hi-C	GSM4698378
Extended Data Figure 2a (row 1, column 3)	312_Wang_HiC_BWX4491_xyl30m_1mM_15m	Hi-C	GSM4698379
Extended Data Figure 2a (row 1, column 4)	313_Wang_HiC_BWX4491_xyl30m_1mM_20m	Hi-C	GSM4698380
Extended Data Figure 2a (row 1, column 5)	314_Wang_HiC_BWX4491_xyl30m_1mM_25m	Hi-C	GSM4698381
Extended Data Figure 2a (row 1, column 6)	315_Wang_HiC_BWX4491_xyl30m_1mM_30m	Hi-C	GSM4698382
Extended Data Figure 2a (row 2, column 1)	304_Wang_HiC_BWX4493_xyl30m_1mM_00m	Hi-C	GSM4698371
Extended Data Figure 2a (row 2, column 2)	305_Wang_HiC_BWX4493_xyl30m_1mM_10m	Hi-C	GSM4698372
Extended Data Figure 2a (row 2, column 3)	306_Wang_HiC_BWX4493_xyl30m_1mM_15m	Hi-C	GSM4698373
Extended Data Figure 2a (row 2, column 4)	307_Wang_HiC_BWX4493_xyl30m_1mM_20m	Hi-C	GSM4698374
Extended Data Figure 2a (row 2, column 5)	308_Wang_HiC_BWX4493_xyl30m_1mM_25m	Hi-C	GSM4698375
Extended Data Figure 2a (row 2, column 6)	309_Wang_HiC_BWX4493_xyl30m_1mM_30m	Hi-C	GSM4698376
Extended Data Figure 2a (row 3, column 1)	316_Wang_HiC_BWX4492_xyl30m_1mM_00m	Hi-C	GSM4698383
Extended Data Figure 2a (row 3, column 2)	317_Wang_HiC_BWX4492_xyl30m_1mM_10m	Hi-C	GSM4698384
Extended Data Figure 2a (row 3, column 3)	318_Wang_HiC_BWX4492_xyl30m_1mM_15m	Hi-C	GSM4698385
Extended Data Figure 2a (row 3, column 4)	319_Wang_HiC_BWX4492_xyl30m_1mM_20m	Hi-C	GSM4698386
Extended Data Figure 2a (row 3, column 5)	320_Wang_HiC_BWX4492_xyl30m_1mM_25m	Hi-C	GSM4698387
Extended Data Figure 2a (row 3, column 6)	321_Wang_HiC_BWX4492_xyl30m_1mM_30m	Hi-C	GSM4698388
Extended Data Figure 2b,c (left)	301_Wang_HiC_BWX4476_1mM_060m	Hi-C	GSM4698368
Extended Data Figure 2b,c (middle)	302_Wang_HiC_BWX4475_1mM_060m	Hi-C	GSM4698369
Extended Data Figure 2b,c (right)	303_Wang_HiC_BWX4463_1mM_060m	Hi-C	GSM4698370
Extended Data Figure 3	303_Wang_HiC_BWX4463_1mM_060m	Hi-C	GSM4698370
Extended Data Figure 4	303_Wang_HiC_BWX4463_1mM_060m	Hi-C	GSM4698370
Extended Data Figure 5	303_Wang_HiC_BWX4463_1mM_060m	Hi-C	GSM4698370
Extended Data Figure 6a (column 1)	340_Wang_HiC_BWX4422	Hi-C	GSM4698407
Extended Data Figure 6a (column 2)	341_Wang_HiC_BWX4423	Hi-C	GSM4698408
Extended Data Figure 6a (column 3)	342_Wang_HiC_BWX4424	Hi-C	GSM4698409
Extended Data Figure 6a (column 4)	343_Wang_HiC_BWX4425	Hi-C	GSM4698410
Extended Data Figure 6a (column 5)	344_Wang_HiC_BWX4870	Hi-C	GSM4698411
Extended Data Figure 6a (column 6)	345_Wang_HiC_BWX4429	Hi-C	GSM4698412
Extended Data Figure 6a (column 7)	346_Wang_HiC_BWX4885	Hi-C	GSM4698413
Extended Data Figure 6b (column 1)	347_Wang_HiC_BWX4891	Hi-C	GSM4698414
Extended Data Figure 6b (column 2)	348_Wang_HiC_BWX5066_0IPTG	Hi-C	GSM4698415
Extended Data Figure 7a (top column 1)	302_Wang_HiC_BWX4475_1mM_060m	Hi-C	GSM4698369
Extended Data Figure 7a (top column 2)	349_Wang_HiC_BWX4475_1mM_090m	Hi-C	GSM4698416
Extended Data Figure 7a (top column 3)	350_Wang_HiC_BWX4475_1mM_120m	Hi-C	GSM4698417
Extended Data Figure 7a (bottom column 1)	351_Wang_HiC_BWX4515_1mM_060m	Hi-C	GSM4698418
Extended Data Figure 7a (bottom column 2)	352_Wang_HiC_BWX4515_1mM_090m	Hi-C	GSM4698419
Extended Data Figure 7a (bottom column 3)	353_Wang_HiC_BWX4515_1mM_120m	Hi-C	GSM4698420
Extended Data Figure 7b (top column 1)	326_Wang_HiC_BWX4883_1mM_060m	Hi-C	GSM4698393
Extended Data Figure 7b (top column 2)	354_Wang_HiC_BWX4883_1mM_090m	Hi-C	GSM4698421
Extended Data Figure 7b (top column 3)	355_Wang_HiC_BWX4883_1mM_120m	Hi-C	GSM4698422
Extended Data Figure 7b (bottom column 1)	328_Wang_HiC_BWX4892_1mM_060m	Hi-C	GSM4698395
Extended Data Figure 7b (bottom column 2)	356_Wang_HiC_BWX4892_1mM_090m	Hi-C	GSM4698423
Extended Data Figure 7b (bottom column 3)	357_Wang_HiC_BWX4892_1mM_120m	Hi-C	GSM4698424
Extended Data Figure 8a (column 1)	366_Wang_input_BWX4462_0IPTG	WGS	GSM4698433

figure	sample	data type	GEO accession number
Extended Data Figure 8a (column 2)	336_Wang_input_BWX4462_1mM_060m	WGS	GSM4698403
Extended Data Figure 8a (column 3)	337_Wang_input_BWX4462_1mM_090m	WGS	GSM4698404
Extended Data Figure 8a (column 4)	338_Wang_input_BWX4462_1mM_120m	WGS	GSM4698405
Extended Data Figure 9a (left)	322_Wang_HiC_BWX4462_1mM_060m	Hi-C	GSM4698389
Extended Data Figure 9a (middle)	331_Wang_HiC_BWX4462_1mM_090m	Hi-C	GSM4698398
Extended Data Figure 9a (right)	332_Wang_HiC_BWX4462_1mM_120m	Hi-C	GSM4698399
Extended Data Figure 9b (left)	358_Wang_HiC_BWX5132_1mM_060m	Hi-C	GSM4698425
Extended Data Figure 9b (middle)	359_Wang_HiC_BWX5132_1mM_090m	Hi-C	GSM4698426
Extended Data Figure 9b (right)	360_Wang_HiC_BWX5132_1mM_120m	Hi-C	GSM4698427
Extended Data Figure 9c (top)	322_Wang_HiC_BWX4462_1mM_060m	Hi-C	GSM4698389
Extended Data Figure 9c (center)	358_Wang_HiC_BWX5132_1mM_060m	Hi-C	GSM4698425
Extended Data Figure 9c (bottom)	331_Wang_HiC_BWX4462_1mM_090m	Hi-C	GSM4698398
Extended Data Figure 10b	01_Rudnerlab_HindIII_HiC_PY79 [9]	Hi-C	GSM2279740
Supplementary Figure 1a	303_Wang_HiC_BWX4463_1mM_060m	Hi-C	GSM4698370
Supplementary Figure 1b	373_Wang_ChIPParB_BWX4462_1mM_060m	ChIP-seq	GSM4859819
Supplementary Figure 1a	336_Wang_input_BWX4462_1mM_060m	WGS	GSM4698403
Supplementary Figure 2c	302_Wang_HiC_BWX4475_1mM_060m	Hi-C	GSM4698369
Supplementary Figure 2c	377_Wang_HiC_BWX4507_1mM_060m	Hi-C	GSM5183861
Supplementary Figure 2c	303_Wang_HiC_BWX4463_1mM_060m	Hi-C	GSM4698370
Supplementary Figure 2c	379_Wang_HiC_BWX4509_1mM_060m	Hi-C	GSM5183863
Supplementary Figure 2c	322_Wang_HiC_BWX4462_1mM_060m	Hi-C	GSM4698389
Supplementary Figure 2c	381_Wang_HiC_BWX4520_1mM_060m	Hi-C	GSM5183865
Supplementary Figure 2c	380_Wang_HiC_BWX4519_1mM_060m	Hi-C	GSM5183864
Supplementary Figure 2c	378_Wang_HiC_BWX4508_1mM_060m	Hi-C	GSM5183862
Supplementary Figure 4	374_Wang_ChIPSMC_BWX3370	ChIP-seq	GSM4859820
Supplementary Figure 4	375_Wang_input_BWX3370	WGS	GSM4859821
Supplementary Figure 5a,b	376_Wang_HiC_BWX4473_1mM_060m	Hi-C	GSM4859822
Supplementary Figure 6a,c	302_Wang_HiC_BWX4475_1mM_060m	Hi-C	GSM4698369
Supplementary Figure 7a,b	303_Wang_HiC_BWX4463_1mM_060m	Hi-C	GSM4698370

Supplementary Table 2. Bacterial strains used in this study.

*E = Extended Data Figure
*S = Supplementary Data Figure

strain	genotype	reference	figure
BWX3221	*parSΔ9 (loxP-spec-loxP), -94˚ parS (loxP-kan-loxP)*	[9]	E1b
BWX3370	*parSΔ9 no a.b., -1˚ parS*	[4]	S4
BWX3377	*parSΔ9 no a.b., -59˚ parS (loxP-kan-loxP)*	[4]	E1b
BWX4359	*yhdG::Phyperspank-(optRBS)-sirA (phleo)*	this study	6
BWX4422	*parSΔ9 no a.b., -27˚ parS, -59˚ parS (loxP-kan-loxP)*	this study	E6a
BWX4423	*parSΔ9 no a.b., -27˚ parS, -94˚ parS (loxP-kan-loxP)*	this study	E6a
BWX4424	*parSΔ9 no a.b., -27˚ parS, -117˚ parS (loxP-kan-loxP)*	this study	E6a
BWX4425	*parSΔ9 no a.b., -27˚ parS, -153˚ parS (loxP-kan-loxP)*	this study	E6a
BWX4428	*parSΔ9 no a.b., -59˚ parS no a.b., -94˚ parS (loxP-kan-loxP)*	this study	E1b
BWX4429	*parSΔ9 no a.b., -59˚ parS no a.b., -117˚ parS (loxP-kan-loxP)*	this study	E6a
BWX4462	*parSΔ9 no a.b., -27˚ parS, -59˚ parS (loxP-kan-loxP), yhdG::Phyperspank-(optRBS)-sirA (phleo)*	this study	3ac; 4abc; S1b; E8ac E9ac
BWX4463	*parSΔ9 no a.b., -59˚ parS no a.b., -94˚ parS (loxP-kan-loxP), yhdG::Phyperspank-(optRBS)-sirA (phleo)*	this study	1c, 2ac, E2bc, S1a, E3, E4, E5, S7ab
BWX4473	*parSΔ9 no a.b., yhdG::Phyperspank-(optRBS)-sirA (phleo)*	this study	S5ab
BWX4475	*parSΔ9 no a.b., -59˚ parS (loxP-kan-loxP), yhdG::Phyperspank-(optRBS)-sirA (phleo)*	this study	1c, E2bc, S6ac, E7a
BWX4476	*parSΔ9 no a.b., -94˚ parS no a.b., yhdG::Phyperspank-(optRBS)-sirA (phleo)*	this study	1c, E2bc

strain	genotype	reference	figure
BWX4479	*parSΔ9 no a.b., -27˚ parS, -94˚ parS (loxP-kan-loxP), yhdG::Phyperspank-(optRBS)-sirA (phleo)*	this study	3a
BWX4480	*parSΔ9 no a.b., -27˚ parS, -117˚ parS (loxP-kan-loxP), yhdG::Phyperspank-(optRBS)-sirA (phleo)*	this study	3a
BWX4481	*parSΔ9 no a.b., -27˚ parS, -153˚ parS (loxP-kan-loxP), yhdG::Phyperspank-(optRBS)-sirA (phleo)*	this study	3a
BWX4482	*parSΔ9 no a.b., -59˚ parS no a.b., -117˚ parS (loxP-kan-loxP), yhdG::Phyperspank-(optRBS)-sirA (phleo)*	this study	3a
BWX4491	*parSΔ9 no a.b., -59˚ parS no a.b., ΔparB(ΔparS) (loxP-spec-loxP), yvbJ::Pspank-(optRBS)-parB(ΔparS) (cat), yhdG::Pxyl-(optRBS)-sirA (phleo)*	this study	1d, E2a
BWX4492	*parSΔ9 no a.b., -94˚ parS no a.b., ΔparB(ΔparS) (loxP-spec-loxP), yvbJ::Pspank-(optRBS)-parB(ΔparS) (cat), yhdG::Pxyl-(optRBS)-sirA (phleo)*	this study	1d, E2a
BWX4493	*parSΔ9 no a.b., -59˚ parS no a.b.,-94˚ parS (loxP-kan-loxP), ΔparB(ΔparS) (loxP-spec-loxP), yvbJ::Pspank-(optRBS)-parB(ΔparS) (cat), yhdG::Pxyl-(optRBS)-sirA (phleo)*	this study	1d, E2a
BWX4507	*parSΔ9 no a.b., -59˚ parS (loxP-kan-loxP), yhdG::Phyperspank-(optRBS)-sirA (phleo), -109˚ (XDS)12 (loxP-spec-loxP)*	this study	S2c
BWX4508	*parSΔ9 no a.b., -27˚ parS, -59˚ parS (loxP-kan-loxP), yhdG::Phyperspank-(optRBS)-sirA (phleo), -109˚ (XDS)12 (loxP-spec-loxP)*	this study	S2c
BWX4509	*parSΔ9 no a.b., -59˚ parS no a.b., -94˚ parS (loxP-kan-loxP), yhdG::Phyperspank-(optRBS)-sirA (phleo), -109˚ (XDS)12 (loxP-spec-loxP)*	this study	S2c
BWX4515	*parSΔ9 no a.b., -91˚ parS (loxP-kan-loxP), yhdG::Phyperspank-(optRBS)-sirA (phleo)*	this study	E7a
BWX4519	*parSΔ9 no a.b., -27˚ parS, -59˚ parS (loxP-kan-loxP), yhdG::Phyperspank-(optRBS)-sirA (phleo), -80˚ (XDS)12 (loxP-spec-loxP)*	this study	S2c
BWX4520	*parSΔ9 no a.b., -27˚ parS, -59˚ parS (loxP-kan-loxP), yhdG::Phyperspank-(optRBS)-sirA (phleo), -19˚ (XDS)12 (loxP-spec-loxP)*	this study	S2c
BWX4547	*yycR (-7˚)::tetO48 (cat), ycgO::PftsW-tetR-cfp (phleo), yhdG::Phyperspank-(optRBS)-sirA (erm)*	this study	4c
BWX4870	*parSΔ9 no a.b., -59˚ parS no a.b., -91˚ parS (loxP-kan-loxP)*	this study	E6a
BWX4883	*parSΔ9 no a.b., -59˚ parS no a.b., -91˚ parS (loxP-kan-loxP), yhdG::Phyperspank-(optRBS)-sirA (phleo)*	this study	3a, E7b
BWX4885	*parSΔ9 no a.b., -91˚ parS no a.b. , -117˚ parS (loxP-kan-loxP)*	this study	E6a
BWX4891	*parSΔ9 no a.b., -59˚ parS no a.b., -91˚ parS no a.b., -117˚ parS (loxP-kan-loxP)*	this study	E6b
BWX4892	*parSΔ9 no a.b., -91˚ parS no a.b. , -117˚ parS (loxP-kan-loxP), yhdG::Phyperspank-(optRBS)-sirA (phleo)*	this study	3a, E7b
BWX4927	*parSΔ9 no a.b., -59˚ parS no a.b., -91˚ parS no a.b., -117˚ parS (loxP-kan-loxP), yhdG::Phyperspank-(optRBS)-sirA (phleo)*	this study	3b
BWX5066	*parSΔ9 no a.b., -27˚ parS, -59˚ parS no a.b., -91˚ parS (loxP-kan-loxP), yhdG::Phyperspank-(optRBS)-sirA (phleo)*	this study	3b, 5ab, E6b
BWX5132	*parSΔ9 no a.b., -27˚ parS, -59˚ parS (loxP-kan-loxP), amyE::Phyperspank-(optRBS)-smc (spec), yhdG::Phyperspank-(optRBS)-scpAB (phleo), yvbJ::Phyperspank-(optRBS)-sirA (erm)*	this study	E9bc
PY79	*wild-type*	[10]	E10b
BNS1615	*parSΔ7: spo0J (parSΔ), yycG (parSΔ) , rocR (parSΔ), cotF (parSΔ), metS (parSΔ), ybbC(parSΔ), ydaD(parSΔ)*	[9]	
BNS1657	*parSΔ8: parB (parSΔ), yycG (parSΔ) , rocR (parSΔ), cotF (parSΔ), metS (parSΔ), ybbC(parSΔ), ydaD(parSΔ), nfrA(parSΔ)*	[11]	
BWX811	*yycR (-7˚)::tetO48 (cat), ycgO::PftsW-tetR-cfp (phleo)*	[12]	
BWX2761	*parSΔ8, ΔparB (ΔparS)::spec*	[9]	
BWX3198	*parSΔ8, +91˚yhaX (ΔparS) (loxP-kan-loxP)*	[9]	
BWX3212	*parSΔ9 no a.b.*	[9]	
BWX3268	*parSΔ9 no a.b., -27˚ parS*	[4]	
BWX3270	*parSΔ9 no a.b., -94˚ no a.b.*	[4]	
BWX3381	*parSΔ9 no a.b., -117˚ parS (loxP-kan-loxP)*	[4]	
BWX3383	*parSΔ9 no a.b., -153˚ parS (loxP-kan-loxP)*	[4]	
BWX3855	*-109˚ (XDS)12 (loxP-spec-loxP)*	[13]	
BWX3858	*-80˚ (XDS)12 (loxP-spec-loxP)*	[13]	
BWX4006	*parSΔ9 no a.b., -1˚ parS no a.b., -19˚ (XDS)12 (loxP-spec-loxP)*	[13]	

Supplementary Table 3. Plasmids used in this study.

plasmid	description	reference
pJW005	*yhdG::Phyperspank-(optRBS)-sirA (phleo)*	[14]
pWX512	*amyE::Phyperspank-(optRBS)-smc (spec)*	this study
pWX722	*yvbJ::Pspank-(optRBS)-parB(ΔparS) (cat)*	[15]
pWX777	*yhdG::Pxyl-(optRBS)-sirA (phleo)*	this study
pWX778	*yhdG::Phyperspank-(optRBS)-scpAB (phleo)*	this study
pWX788	*yhdG::Phyperspank-(optRBS)-sirA (erm)*	this study

Supplementary Table 4. Oligonucleotides used in this study.

oligos	sequence	use
oML87	ccagaagtttctcagagtcgg	pWX777
oWX428	ggagcttttcaaaaagtgctgaaacgc	pWX778
oWX438	gaccagggagcactggtcaac	BWX3379
oWX486	gccgctctagctaagcagaaggc	pWX512, pWX778, pWX788
oWX487	aacggtctgataagagacaccggc	pWX778
oWX516	cgcgctagcacataaggaggaactactatgttcctcaaacgtttagac	pWX512
oWX517	tttgcatgcttactgaacgaattcttttgtttcttcc	pWX512
oWX524	ggtacgtacgatctttcagccgactc	pWX512, pWX788
oWX848	gaagagctctctgccgtatctgaaaag	pWX512
oWX1194	gggaaagtggaagagatcctgagc	pWX512
oWX1195	cttcacaatgaaaatgtcgaagag	pWX512
oWX1196	gcccggcattcatcatttctcggg	pWX512
oWX1241	ctcgagtgttacacgtgaaacatccttctgctccctcgctcag	BWX3379
oWX1279	ctaatccgacagctaacctcgtaggcg	BWX3379
oWX1280	tgtttcacgtgtaacactcgagtcaccctgtaaacacttcgccatc	BWX3379
oWX1281	gttgaccagtgctccctggtctatcaaaaaaatccggcgtgcagtcg	BWX3379
oWX1282	cgataaagtcggaccagggatgctcgg	BWX3379
oWX1283	tcctattttcaggcagtgacgccg	BWX3379
oWX1284	acctctgcccaatcttacgtcggc	BWX3379
oWX1892	gaatgaagcttacataaggaggaactactatggaacgtcactactatacgtac	pWX777, pWX788
oWX1893	gagatgctagccggttttagacaaaatttctttctttcaccgg	pWX777, pWX788
oWX1894	acatagtacatagcgaatcttccc	pWX777
oWX1897	gaatgaagcttacataaggaggaactactatggaagaatatcaagtgaaaattg	pWX778
oWX1898	atgctagcctattttatatcttcgaaggtttggttaaag	pWX778

Supplementary References

1 Harris, C. R. *et al.* Array programming with NumPy. *Nature* **585**, 357-362, doi:10.1038/s41586-020-2649-2 (2020).

2 Banigan, E. J., van den Berg, A. A., Brandao, H. B., Marko, J. F. & Mirny, L. A. Chromosome organization by one-sided and two-sided loop extrusion. *eLife* **9**, doi:10.7554/eLife.53558 (2020).

3 Brandao, H. B. *et al.* RNA polymerases as moving barriers to condensin loop extrusion. *Proc Natl Acad Sci U S A* **116**, 20489-20499, doi:10.1073/pnas.1907009116 (2019).

4 Wang, X., Brandao, H. B., Le, T. B., Laub, M. T. & Rudner, D. Z. Bacillus subtilis SMC complexes juxtapose chromosome arms as they travel from origin to terminus. *Science* **355**, 524-527, doi:10.1126/science.aai8982 (2017).

5 Imakaev, M., Goloborodko, A. & Brandao, H. B. in *Zenodo* (2019).

6 Eastman, P. *et al.* OpenMM 7: Rapid development of high performance algorithms for molecular dynamics. *PLoS Comput Biol* **13**, e1005659, doi:10.1371/journal.pcbi.1005659 (2017).

7 Virtanen, P. *et al.* SciPy 1.0: fundamental algorithms for scientific computing in Python. *Nat Methods* **17**, 261-272, doi:10.1038/s41592-019-0686-2 (2020).

8 Kim, E., Kerssemakers, J., Shaltiel, I. A., Haering, C. H. & Dekker, C. DNA-loop extruding condensin complexes can traverse one another. *Nature* **579**, 438-442, doi:10.1038/s41586-020-2067-5 (2020).

9 Wang, X. *et al.* Condensin promotes the juxtaposition of DNA flanking its loading site in Bacillus subtilis. *Genes Dev* **29**, 1661-1675, doi:10.1101/gad.265876.115 (2015).

10 Youngman, P. J., Perkins, J. B. & Losick, R. Genetic transposition and insertional mutagenesis in Bacillus subtilis with Streptococcus faecalis transposon Tn917. *Proc Natl Acad Sci U S A* **80**, 2305-2309 (1983).

11 Sullivan, N. L., Marquis, K. A. & Rudner, D. Z. Recruitment of SMC by ParB-parS organizes the origin region and promotes efficient chromosome segregation. *Cell* **137**, 697-707, doi:10.1016/j.cell.2009.04.044 (2009).

12 Wang, X., Montero Llopis, P. & Rudner, D. Z. Bacillus subtilis chromosome organization oscillates between two distinct patterns. *Proc Natl Acad Sci U S A*, doi:10.1073/pnas.1407461111 (2014).

13 Karaboja, X. *et al.* XerD unloads bacterial SMC complexes at the replication terminus. *Mol Cell* **81**, 756-766 (2021).

14 Wagner, J. K., Marquis, K. A. & Rudner, D. Z. SirA enforces diploidy by inhibiting the replication initiator DnaA during spore formation in Bacillus subtilis. *Mol Microbiol* **73**, 963-974, doi:MMI6825 [pii] 10.1111/j.1365-2958.2009.06825.x (2009).

15 Wang, X. *et al.* In Vivo Evidence for ATPase-Dependent DNA Translocation by the Bacillus subtilis SMC Condensin Complex. *Mol Cell* **71**, 841-847 e845, doi:10.1016/j.molcel.2018.07.006 (2018).